JOURNAL OF GEOPHYSICAL RESEARCH, VOL. 111, D18210, doi:10.1029/2005JD006967, 2006

Polar stratospheric ice cloud above Spitsbergen

Marion Maturilli[1] and Andreas Dörnbrack[2]

Received 8 December 2005; revised 12 April 2006; accepted 24 May 2006; published 28 September 2006.

[1] Within the extremely cold and stable polar vortex of winter 2004–2005 a polar stratospheric ice cloud was observed from Ny-Ålesund (Spitsbergen) on 26 January 2005. The observation of a cloud with backscatter ratios up to 23 and volume depolarization larger than 50% is unique in our 15 year ground-based lidar data record. Simultaneous balloon-borne water vapor measurements indicate the presence of mesoscale ice clouds nearby. Normally, low horizontal wind speeds inside the inner vortex prevent vertical wave propagation. However, the rare coincidence of different meteorological processes occurring during a poleward-breaking Rossby wave event caused favorable conditions for the vertical propagation of mountain waves excited by the flow past Spitsbergen. Detailed meteorological analysis shows that the ice particle formation processes on 26 January 2005 were most likely provoked by mesoscale stratospheric temperature anomalies, leading to a local reduction in water vapor.

Citation: Maturilli, M., and A. Dörnbrack (2006), Polar stratospheric ice cloud above Spitsbergen, *J. Geophys. Res.*, *111*, D18210, doi:10.1029/2005JD006967.

1. Introduction

[2] Every winter, the large-scale radiative cooling of the air inside the southern hemispheric polar vortex enables the existence of stratospheric ice clouds, so-called polar stratospheric clouds (PSCs) of type II. Heterogeneous chemical reactions on the ice PSC particles convert effectively inert reservoir gases to photochemically active species that drive the catalytic ozone destruction [*Solomon*, 1999]. Additionally, ice PSCs remove trace gases such as water (H_2O) and nitric acid (HNO_3) temporarily from the gas phase by condensation and freezing. The ice cloud particles may grow to larger sizes and, eventually, transport the particle bound trace gas components downward due to gravitational settling. Hence PSCs of type II can irreversibly remove H_2O and HNO_3 from higher altitudes (dehydration and denitrification, respectively). Under denitrified conditions, ozone depletion can be prolonged and the springtime ozone loss is enhanced [*Rex et al.*, 1997; *Waibel et al.*, 1999]. In the Antarctic, dehydration is regularly observed on a large scale [*Nedoluha et al.*, 2000, 2002] as vortex temperatures are low enough over a long period for the widespread occurrence of ice PSCs every winter. Distinctively, in the Arctic, dehydration is found to a much lesser extent and is commonly linked to single events [e.g., *Vömel et al.*, 1997; *Herman et al.*, 2002; *Schiller et al.*, 2002].

[3] The majority of Arctic ice PSC observations by ground-based, balloon-borne and airborne instruments is documented for Scandinavia [*Hansen and Hoppe*, 1997; *Carslaw et al.*, 1998a; *Wirth et al.*, 1999; *Kivi et al.*, 2001; *Dörnbrack et al.*, 2002; *Fueglistaler et al.*, 2003; *Reichardt et al.*, 2004]. In fact, Arctic ice PSCs have only been observed in regions of additional mesoscale cooling caused by internal gravity waves [e.g., *Hitchman et al.*, 2003]. Gravity waves with amplitudes large enough to reduce the temperature significantly below the ice frost point T_{ice} were predominantly excited orographically [e.g., *Dörnbrack et al.*, 1999]. Since strong and nearly unidirectional winds throughout the troposphere and stratosphere favor the upward wave propagation, mountain wave-induced stratospheric temperature fluctuations leading to PSC formation are enhanced at the inner edge of the polar vortex [*Dörnbrack and Leutbecher*, 2001]. Alternatively, PSCs can be induced by jet stream instabilities in breaking Rossby waves and by shear instabilities in the tropopause region [*Teitelbaum et al.*, 2001; *Hitchman et al.*, 2003; *Buss et al.*, 2004].

[4] In this paper, we present a unique lidar observation of an ice PSC at the German Koldewey station in Ny-Ålesund (78.9°N, 11.9°E), Spitsbergen, in combination with nearly simultaneous balloon-borne stratospheric water vapor measurements. During the time of observation on 26 January 2005, the polar vortex was extremely cold. Temperatures of 1–2 K below the ice frost point T_{ice} were achieved in the cold pool by radiative cooling as well as by the adiabatic cooling of ascending air parcels in a planetary wave (as described by *Teitelbaum and Sadourny* [1998]). However, as synoptic-scale temperatures were close to T_{ice}, additional cooling through mesoscale processes might be required to explain the formation of the ice PSC particles.

[5] A thorough analysis of the meteorological conditions discusses large-scale cooling processes inside the Arctic vortex. In addition, we investigate whether mesoscale atmospheric processes such as inertia-gravity and mountain waves induced favorable formation conditions for ice particles locally above Spitsbergen. In the next section, we

[1] Alfred Wegener Institute for Polar and Marine Research, Potsdam, Germany.
[2] Institut für Physik der Atmosphäre, Deutsches Zentrum für Luft- und Raumfahrt, Oberpfaffenhofen, Germany.

0148-0227/06/2005JD006967$09.00

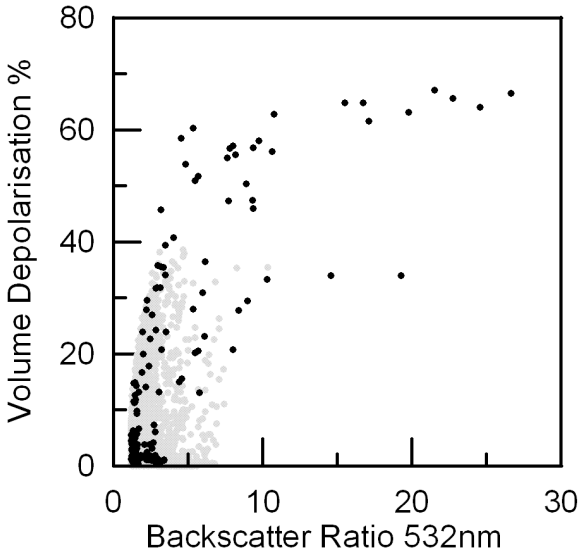

Figure 1. Aerosol backscatter ratio at 532 nm and volume depolarization of all polar stratospheric cloud (PSC) data points from 10 min integration profiles retrieved by the German lidar in Ny-Ålesund, Spitsbergen, between 1991–1992 and 2004–2005. The total number of PSC data points from 10 min integrated profiles with 150 m vertical resolution (shaded points) is larger than 50.000, while the observation on 26 January 2005 (solid points) accounts for 180 data points.

present the ice PSC observation and related measurements in Ny-Ålesund on 26 January 2005. Section 3 describes the large-scale meteorological situation in the stratosphere whereas section 4 investigates the impact of smaller-scale meteorological processes on the stratospheric temperature distribution by means of mesoscale numerical simulations. Section 5 discusses different formation scenarios for the observed ice PSC and, section 6 concludes the paper.

2. Polar Stratospheric Cloud (PSC) Observations

2.1. Ny-Ålesund Lidar Data Record of PSC Observations

[6] The lidar system at the German Koldewey station in Ny-Ålesund is operational since the winter 1988–1989. Stratospheric aerosol backscatter and depolarization measurements at a wavelength of 532 nm have been regularly performed every winter since 1991 whenever the tropospheric cloud cover allowed for [*Beyerle et al.*, 1994; *Biele et al.*, 2001; *Massoli et al.*, 2006]. In total, the Ny-Ålesund lidar record represents the longest continuous lidar PSC record in the Arctic region. Figure 1 shows the backscatter ratio $R_{532\text{nm}}$ and the volume depolarization $\delta_{532\text{nm}}$ of all PSC data retrieved between 1991–1992 and 2004–2005. The standard 10 min integration profiles with 150 m vertical resolution limited to $R_{532\text{nm}} > 1.2$ result in more than 50,000 PSC data points. The observation of the 26 January 2005 (180 PSC data points) clearly stand out against all our previous measurements.

[7] Recently, a representative subset of these data has been classified [*Massoli et al.*, 2006] by applying the common lidar PSC classification scheme [*Browell et al.*, 1990; *Toon et al.*, 1990] with extensions for subtypes. Liquid PSCs, characterized by low depolarization, occurred in 37% of our observations, while 25% of the PSCs were identified as consisting of depolarizing solid nitric acid trihydrate (NAT) particles with small backscatter ratio $R_{532\text{nm}} < 1.56$. A large group of PSCs (31%) was composed of mixed (liquid/solid) particles associated with their intermediate backscatter and depolarization characteristics. Only 4% of all PSC data were so-called NAT enhanced PSCs [after *Tsias et al.*, 1999], being solid NAT particles with high backscatter ratio $R_{532\text{nm}} > 1.56$. However, a PSC of type II with a backscatter ratio of $R_{532\text{nm}} > 10$ and volume depolarization $\delta_{532\text{nm}} > 50\%$ had never been identified in the complete data record prior to 26 January 2005 (Figure 1). Before we discuss this unique PSC observation in detail, the radiosonde temperatures are presented next.

2.2. Temperature Measurements on 26 January 2005

[8] The ambient stratospheric temperature T was measured with a F-Thermocap sensor by a standard RS-92 radiosonde launched from Ny-Ålesund on 26 January 2005 at 2300 UTC. The uncertainty of the temperature observation was ±0.3 K in the lower stratosphere. Figure 2a shows the stratospheric temperature measured during ascent near Ny-Ålesund at 2330 UTC. Temperatures as low as 183 K have been detected at about 22 km altitude. A radiosonde measurement 12 hours earlier (shaded line in Figure 2a) shows a temperature minimum of 184 K below this level but up to 4 K warmer temperatures compared to the 2330 UTC measurement in the altitude range between 19 and 22 km.

[9] The temperature difference $T - T_{\text{ice}}$ is shown in Figure 2b whereby the ice frost point T_{ice} was calculated applying a formula for the saturation water vapor pressure recently developed by *Murphy and Koop* [2005] and assuming a water vapor profile as sketched by the dashed line in Figure 2d. This undisturbed H_2O profile may represent the conditions upstream of Spitsbergen and near the location of PSC nucleation. Additionally, the temperature difference to T_{ice} was calculated using the observed disturbed H_2O profile (solid lines in Figures 2b and 2d). The water vapor measurements will be discussed in more detail in section 2.4. Combined, the temperature profiles reveal a cold layer with $T < T_{\text{ice}}$ between 18.5 and 22.5 km altitude. Inside this cold layer, the observed temperatures dropped up to ≈3 K below T_{ice} near 20.8 km and 22 km altitude, respectively.

[10] Please note that the region with $T < T_{\text{ice}}$ is capped by a narrow inversion layer with a local maximum of the buoyancy frequency $N = (g/\Theta \cdot \partial\Theta/\partial z)^{1/2} \approx 0.04\ \text{s}^{-1}$, where g is the gravitational acceleration and Θ denotes the potential temperature. A mixing layer with strongly reduced values of $N \approx 0.005\ \text{s}^{-1}$ is located beneath this capping inversion. Here, we can only speculate that this structure constitutes the signature of overturning gravity waves [e.g., *Dörnbrack*, 1998].

2.3. Lidar Measurements of an Ice PSC

[11] Vertical profiles of the backscatter ratio $R_{532\text{nm}}$ and the volume depolarization $\delta_{532\text{nm}}$ of 40 min of lidar measurements on 26 January 2005 between 1855 and 1934 UTC are shown in Figure 2c. Unfavorable weather conditions

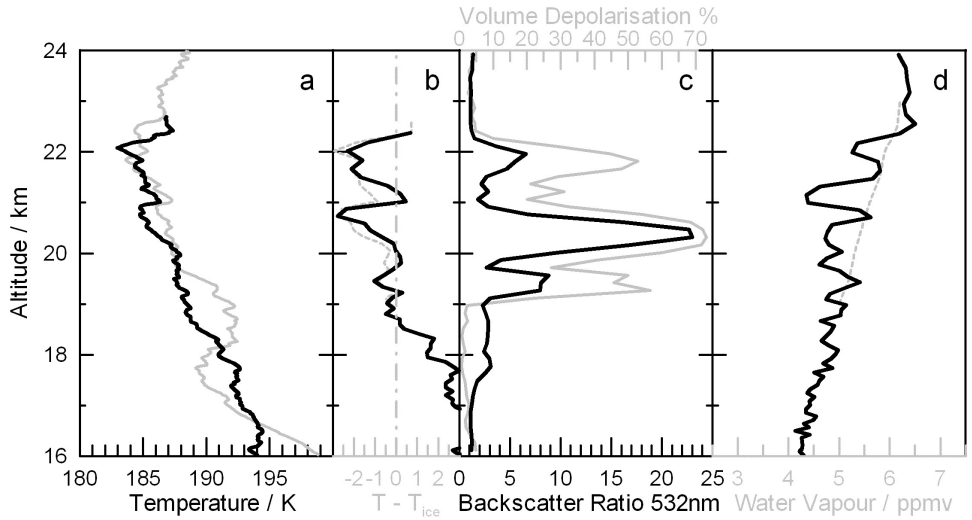

Figure 2. Measurements on 26 January 2005 in Ny-Ålesund. (a) Radiosonde temperature at 1100 UTC (shaded line) and 2300 UTC (solid line). (b) Temperature difference $T - T_{ice}$ (T_{ice} calculated after *Murphy and Koop* [2005]) for the 2300 UTC radiosonde temperature and the water vapor profiles shown in Figure 2d for the FLASH-B measurement (solid line) and the anticipated q_{H20} profile (dashed shaded line), respectively. (c) Aerosol backscatter ratio (solid line, lower axis) and volume depolarization (shaded line, upper axis) at 532 nm, integrated between 1855 and 1934 UTC. (d) Water vapor mixing ratio q_{H20} as measured by FLASH-B hygrometer at 2000 UTC. The straight shaded line indicates the anticipated mean increase of q_{H20} under undisturbed conditions. The height of the q_{H20} profile was calculated by integrating the hydrostatic equation using a mean value of the temperature taken from the 1100 UTC and 2300 UTC soundings.

with low cloud cover before and after that period prevented longer PSC measurements on that day (readers interested in the tropospheric weather situation are referred to Appendix A).

[12] A thick polar stratospheric cloud with $R_{532nm} > 2$ was measured between 17 and 22 km altitude. Volume depolarization values $\delta_{532nm} < 1.44\%$ classify the lower part of this cloud ($z < 19$ km) as a PSC composed of liquid particles. Volume depolarization values larger than 35% were measured in three distinct regions around 19.5 km, 20.5 km, and 22 km altitude, together with $R_{532nm} > 5$, respectively. Maximum values of $\delta_{532nm} \approx 70\%$ and $R_{532nm} \approx 23$ were attained between 20 and 21 km altitude. Using the PSC classification schemes by *Browell et al.* [1990] and *Toon et al.* [1990], we unambiguously identify this middle layer as type II PSC or polar stratospheric ice cloud. This ice layer was detected in a temperature range up to 3 K below T_{ice}, and thus under conditions of ice supersaturation.

[13] Although the both neighboring layers revealed lower backscatter values, their respective depolarization values of $\delta_{532nm} \geq 50\%$ were unusually large. These layers may be classified as NAT enhanced PSCs. Such clouds were frequently observed downwind of ice PSCs [*Carslaw et al.*, 1998b; *Hu et al.*, 2002] or in their close vicinity [*Wirth et al.*, 1999]. Here, however, temperatures near and below T_{ice} in concert with optical calculations (B. Luo, personal communication, 2005) and the water vapor measurements (Figure 2d) suggest that these layers might be composed of ice particles (thin PSCs of type II). Ice PSCs are rarely found in thermodynamical equilibrium (i.e., at $T = T_{ice}$), but were measured at a range of ice supersaturations [*Luo et al.*, 2003; *Fueglistaler et al.*, 2003]. Hence we do not assume a fully developed and thick ice cloud. Instead, the cloud layers around the unambiguously identified ice PSC may consist of growing or evaporating ice particles depending on their temperature history, the ambient meteorological conditions, and the availability of trace gases. In between these layers, depolarizing particles with low backscatter ratio ($R_{532nm} \approx 1.5$) indicate PSCs of type Ia. In the following, we concentrate on the discussion of the ice PSC layer at around 20 km altitude.

2.4. Water Vapor Observation

[14] Around 2000 UTC, a balloon-borne Lyman-α hygrometer "FLASH-B" [*Yushkov et al.*, 1998, 2001] measured the stratospheric water vapor profile with an uncertainty of ±8% and a vertical resolution of about 150 m in the PSC altitude range (Figure 2d). To avoid contamination effects caused by tropospheric remnants in the plume of the balloon, only the descent data about 100 km southeast of Ny-Ålesund are shown. Between 16 and 24 km altitude, the water vapor mixing ratio q_{H2O} gradually increases with altitude as expected for inner vortex conditions. In three distinct layers between 19.5 and 22.5 km altitude, water vapor was depleted by up to 1.5 ppmv below the undisturbed values.

[15] While we cannot completely exclude that the minima in the water vapor concentration represent permanent removal of water vapor, we argue that the laminated structure of the H_2O concentration may reflect the local partitioning of water into ice particles, or measurements in an ice PSC. This view is supported by the strong corre-

lation between the three maxima in the backscatter profile and the three minima in the water vapor profile. The vertical shift of about 500 m between the lower two water vapor minima and the maxima in the backscatter ratios might be explained by the drift of the hygrometer balloon, hence, the detection of the water vapor profile about 100 km downwind southeast of the lidar PSC observation above Ny-Ålesund.

[16] Altogether, the measurements of temperature, backscatter ratio, volume depolarization and water vapor concentration show that stratospheric ice clouds were detected at temperatures below T_{ice}. In the following, we discuss the meteorological situation in winter 2004–2005 and, particularly, we concentrate on 26 January 2005 in order to explain this unique observation of an ice PSC above Spitsbergen.

3. Synoptic-Scale Analyses

[17] In winter 2004–2005, the Arctic polar vortex was exceptionally long-lasting and cold from its early formation onward [e.g., *Kleinböhl et al.*, 2005; *Manney et al.*, 2006]. At higher stratospheric levels ($\Theta > 550$ K, $p < 30$ hPa, $z > 22$ km), temperatures allowed the existence of NAT PSCs already in late November 2004. Temperatures on the 475 K isentropic surface ($p \approx 50$ hPa, $z \approx 19$ km) were below the NAT threshold from December 2004 onward. In addition, the stratospheric temperature fell below the ice frost point on several single days around the turn of the year, at the end of January, and in the second half of February 2005. Most prominent, one week period end of January 2005 revealed the largest potential ice PSC area in the Arctic ever calculated from ECMWF analyses so far (P. von der Gathen, personal communication, 2005).

[18] In this particular period, the polar vortex was kidney shaped and mostly barotropic. A displacement between the geopotential height and the temperature field (disturbance of the Arctic vortex by a synoptic wave) occurred between Greenland and the Norwegian Sea and was caused by an underlying anticyclone elevating the tropopause and the stratospheric levels above. On the basis of T511/L60 operational ECMWF analyses valid on 26 January 2005, the very cold area with $T < T_{ice}$ extended from the North Pole to about the latitude of Sodankylä, Finland (~67°N) reaching from 30°W to about 65°E. The Spitsbergen area was characterized by a rather uniform temperature field of ~188 K at 50 hPa and ~185 K at the 30 hPa level, both levels being about 1 K below T_{ice} (Figure 3).

[19] In order to investigate the temperature history of the air mass sampled at Ny-Ålesund, backward trajectories were calculated, with starting points on different pressure levels located at 79°N and 12°E on 26 January 2005, 2100 UTC. The applied trajectory scheme LAGRANTO [*Wernli and Davis*, 1997] was run with meteorological data provided by T511/L60 operational ECMWF data interpolated on a regular 0.5° × 0.5° latitude-longitude grid every 3 hours (6 hourly operational analyses at meteorological standard times plus t_0 + 3 hours and t_0 + 9 hours predictions at the intermediate steps based on the forecasts initialized at t_0 = 0000 UTC and t_0 = 1200 UTC, respectively) (see Figure 3).

[20] All backward trajectories passed the Atlantic in the first 12 hours and crossed Greenland's east coast at about 78°N. Note that the mesoscale stratospheric temperature anomalies above Greenland's east coast and downstream occurred predominantly at lower latitudes. Thus air parcels arriving at Ny-Ålesund were not strongly influenced by the extreme low temperatures further south with an absolute minimum of 176.5 K at 30 hPa. Instead, the most prominent cooling of the air parcels by about ΔT = 8 K occurred slowly during the 36 hours prior to the observation. Inspection of the pressure change along the trajectories suggests that this slow cooling is caused by large-scale adiabatic lifting of air induced by an underlying tropospheric high-pressure ridge. However, only about 12 hours prior to the observations the temperature drops below T_{ice}, with $T - T_{ice}$ always less than 2 K.

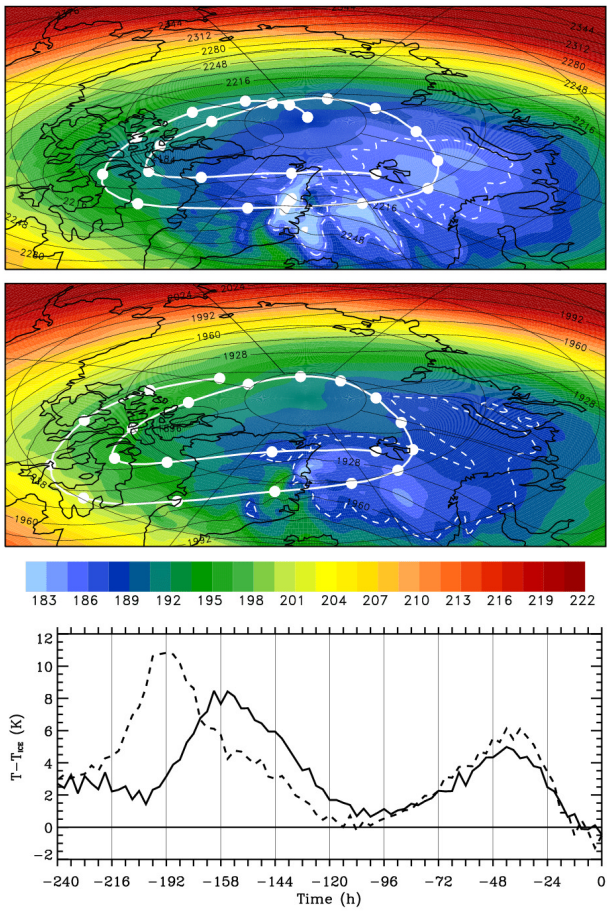

Figure 3. Temperature (color shading, K), T_{ice} calculated with q_{H2O} = 5 ppmv (dashed white contour line) and geopotential height (solid lines, dam) at the (top) 30 hPa and (middle) 50 hPa pressure levels, valid on 26 January 2005 at 1800 UTC. Data are based on operational T511/L60 European Centre for Medium-Range Weather Forecasts (ECMWF) analyses interpolated on a regular 0.5° × 0.5° latitude-longitude grid. The 10 day backward trajectories launched at 2100 UTC are plotted in white, a dot every 12 hours. (bottom) $T - T_{ice}$ for the trajectories released at 30 hPa (solid line) and 50 hPa (dashed line).

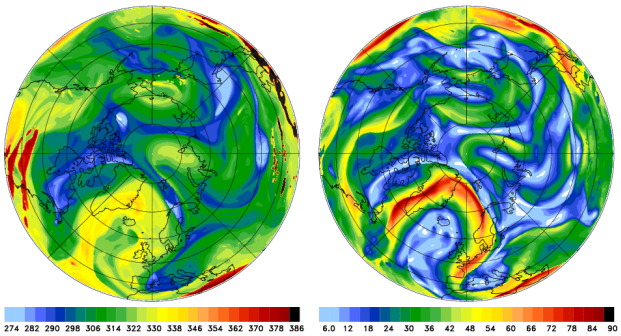

Figure 4. ECMWF-analyzed tropopause maps valid on 26 January 2005 at 1200 UTC: (left) potential temperature (K) and (right) horizontal wind speed (m/s) at the dynamical tropopause defined by the 2 PVU surface; 1 PVU = 10^{-6} m^2 s^{-1} K kg^{-1} (see, e.g., *Holton et al.* [1995] PV definitions of the dynamical tropopause in the literature range from 1.5 to 3.5 PVU).

[21] In the next section we investigate the possible impact of mesoscale processes on the stratospheric temperature field.

4. Mesoscale Perturbations of the Stratospheric Temperature Field

4.1. Inertia-Gravity Waves

[22] The large-scale synoptic situation before and during the PSC observation was characterized by a so-called P2-type breaking Rossby wave event [*Peters and Waugh*, 1996]: a broad extrusion of subtropical tropospheric air spreading northeast and wrapping itself up anticyclonically, forming a large anticyclone over the Atlantic which extended up to a latitude of 80°N on 26 January 2005. On the ECMWF tropopause maps [*Morgan and Nielsen-Gammon*, 1998] shown in Figure 4, the anticyclone with an elevated tropopause is marked by large values of potential temperature Θ. Sharp Θ gradients are associated with the tropopause jet forming a Ω-shaped ring of high horizontal wind speeds around the anticyclone. Exceptionally, Spitsbergen is located directly at the edge of this tropopause jet.

[23] A strongly anticyclonically curved jet is not geostrophically balanced. In order to maintain this state, the relationship between the mass and the velocity field is adjusted by radiating inertia-gravity waves ("Rossby adjustment problem" [see *Gill*, 1982; *O'Sullivan and Dunkerton*, 1995; *Plougonven et al.*, 2003]). Subsequently, these waves propagate vertically and horizontally and are able to modulate the temperature field in the upper troposphere [e.g., *Spichtinger et al.*, 2005] and lower stratosphere [e.g., *Hitchman et al.*, 2003].

[24] In order to investigate if the jet stream located west of Spitsbergen (compare Figure 4) excited inertia-gravity waves on 26 January 2005, we inspected horizontal and vertical sections of the divergence of the horizontal wind speed based on operational T511/L60 ECMWF analyses as suggested by *Plougonven and Teitelbaum* [2003]. The vertical cross section perpendicular to the jet axis, shown in Figure 5, exemplifies the situation: above the eastern flank of the jet stream (maximum $V_H \approx 80$ m/s) alternating bands of positive and negative divergence mark the presence of inertia-gravity waves. Their phase lines are aligned parallel to the jet axis, and typical vertical and horizontal wavelengths as determined from the ECMWF analyses amount to $\lambda_z \approx 3$ km and $\lambda_H \approx 200$ km, respectively. Above Spitsbergen and about 200 km east of the jet axis, the local temperature within the stratospheric cold layer was reduced by about $\Delta T = 2$ K to $T = 184$ K ($\approx$2 K below T_{ice}).

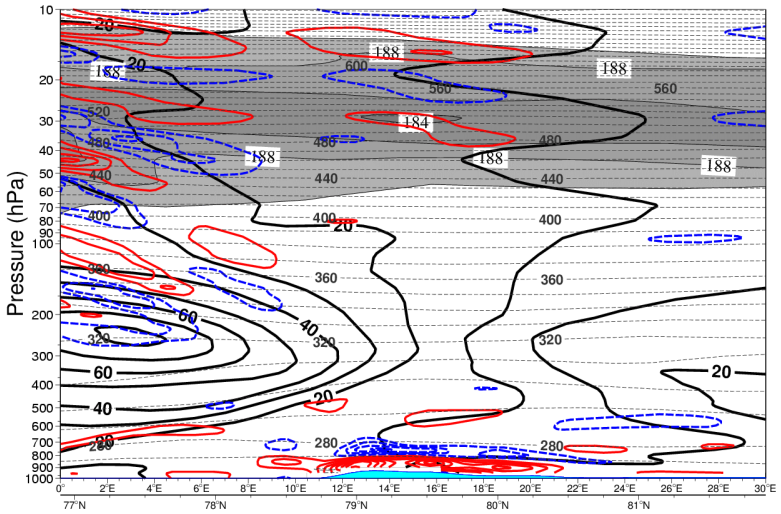

Figure 5. Vertical cross section perpendicular to the jet axis. Magnitude of the horizontal wind speed $V_H \geq 10$ m/s (bold lines, m/s; $\Delta V_H = 10$ m/s), potential temperature (shaded dashed lines, K; $\Delta\Theta = 10$ K), and divergence of the horizontal wind (blue/red contour lines, 10^{-5} s^{-1}; lowest contour lines at $\pm 1 \times 10^{-5}$ s^{-1}, respectively; the contour increment is 1×10^{-5} s^{-1}). The stratospheric cold layer with $T < 190$ K is shaded with superimposed contour lines of absolute temperature (K, $\Delta T = 2$ K). Data are from T511/L60 ECMWF operational analyses interpolated on a regular 0.5° × 0.5° latitude-longitude grid valid on 26 January 2005 at 1200 UTC.

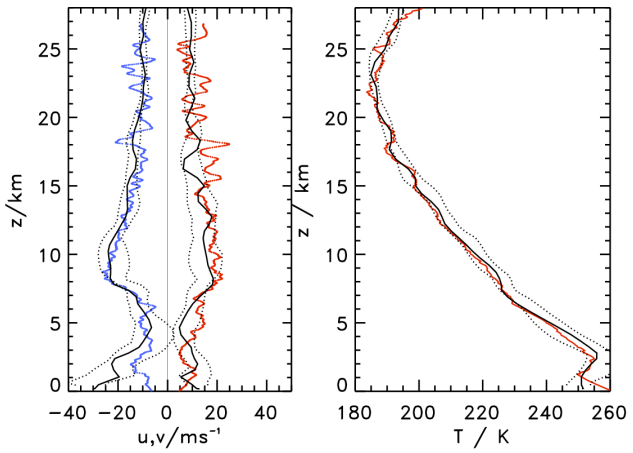

Figure 6. (left) Zonal and meridional velocity components u and v (red and blue solid lines, respectively) and (right) absolute temperature T (red line) as observed by the radio sounding released in Ny-Ålesund at 1100 UTC on 26 January 2005. The solid lines show the same quantities as retrieved from a virtual balloon sounding based on a forward trajectory calculation using the MM5 results from the nested domain with the assumption of a mean balloon ascent rate of 4 m/s; the dashed lines mark the minima and maxima of u, v, and T based on 81 virtual balloon soundings released from an array of 9 × 9 grid points separated by Δx = 4 km around Ny-Ålesund.

Maximum values of the horizontal divergence, i.e., of inertia-gravity wave activity occurred in the period before local noon on 26 January 2005.

[25] In order to simulate inertia-gravity wave excitation and propagation with higher horizontal and vertical resolutions, we performed a set of mesoscale numerical experiments using the nonhydrostatic weather prediction model MM5 (for the setup see Appendix B). The mesoscale model MM5 has been successively used to simulate the dynamics of inertia-gravity waves [e.g., *Dörnbrack et al.*, 1999, 2002; *Zhang*, 2004; *Zülicke and Peters*, 2006].

[26] A comparison of the 1100 UTC radio sounding with the mesoscale simulation results shows a close correspondence of the stratospheric wind and temperature fields (Figure 6). The numerical results are based on 81 virtual balloon soundings released at horizontal locations in a grid of 36 × 36 km^2 surrounding Ny-Ålesund, tracing the horizontal velocity components and the temperature. In general, the vertical profiles of the simulated quantities agree well with the stratospheric observations, and even the wave structure in the temperature sounding between 15 and 21 km altitude can be reproduced. However, it becomes also evident that the wind and temperature fluctuations between 18 and 24 km altitude with typical vertical wavelengths less than 1000 m (which might be the results of smaller-scale instabilities) cannot be resolved with a vertical resolution of z = 200 m [see *Leutbecher and Volkert*, 2000].

[27] Figure 7 shows the simulated stratospheric temperature distribution at 20 km altitude at 0600, 1200, 1700, and 2100 UTC (+18, +24, +29, and +33 hour simulation time after MM5 initialization), respectively. The horizontal section at 0600 UTC reveals a significant perturbation of the stratospheric temperature field due to inertia-gravity waves, visible as temperature fluctuations with phase lines nearly parallel to the axis of the jet stream, above and east of Spitsbergen, λ_H being 200 km close to the jet axis and becoming shorter toward east. The peak-to-peak amplitude of the temperature fluctuations $\Delta T \approx 4$ K is reduced with increasing distance from the jet axis. This is in accordance with inertia-gravity waves being confined to the vicinity of the jet stream due to horizontal wave refraction [see, e.g., *Dunkerton*, 1984; *O'Sullivan and Dunkerton*, 1995]. The mesoscale simulations confirm that Spitsbergen is mainly influenced by inertia-gravity waves in the morning of 26 January 2005. After this time, the phase lines of the simulated waves became gradually perpendicular to the jet axis and the temperature fluctuations grew significantly at all stratospheric levels (Figure 7). This change of the orientation of the phase lines indicates another source of wave-induced stratospheric temperature fluctuations, namely, mountain waves.

4.2. Mountain Waves

[28] The mesoscale simulation shows that mountain waves were excited during the entire day until about 1800 UTC due to a strong postfrontal northwesterly wind passing Spitsbergen. However, favorable propagation conditions for waves (i.e., nearly unidirectional winds in troposphere and stratosphere) occurred just after about 0600 UTC, when the anticyclone extended very far north and the axis of the associated tropopause jet shifted above the western flank of Spitsbergen (compare Figure 4). Eventually, the northwesterly wind direction of the jet stream was aligned with the near-surface winds as displayed by the wind vectors parallel to the contour lines of geopotential height at 900 hPa (see Figure 7). During the day, the 900 hPa contour line separation became wider (corresponding to weaker winds) and, finally, at about 1800 UTC the lower tropospheric wind turned to southwesterlies after the passage of the ridge axis, in agreement with the observed wind of the 2300 UTC radiosonde measurement. At this time, mountain wave excitation was reduced, and the diminishing tropospheric wind speed as well as the large-scale descent in the anticyclone degraded the favorable wave propagation conditions. Thus mountain waves exclusively modulated the stratospheric temperature field during the afternoon of 26 January 2005.

[29] Figure 8 displays this modulation by jet-parallel vertical cross sections of T, Θ, and the vertical wind speed at the corresponding times as in Figure 7. At 1200 UTC, the waves just commenced to modulate the cold stratospheric layer (see Figures 7 and 8). The mountain waves have typical characteristics of vertically propagating hydrostatic gravity waves in the nonrotating limit: $\lambda_H < 50$ km and $\lambda_z \approx$ 6 to 8 km. The horizontal temperature field at stratospheric levels consist of numerous patches of localized cooling whereby $T_{\mathrm{MIN}} \approx 184$ K (see Figure 7, 1700 UTC). These fast-propagating waves seem to be excited at individual ridges of the model orography. Linear wave theory predicts a vertical group velocity $c_{gz} = V_H^2 k_H / N$ [*Gill*, 1982] of about 5.65 ms^{-1}, where $k_H = 2\pi/\lambda_H$ is the horizontal component of the wave vector, i.e., to reach a height of 22 km these

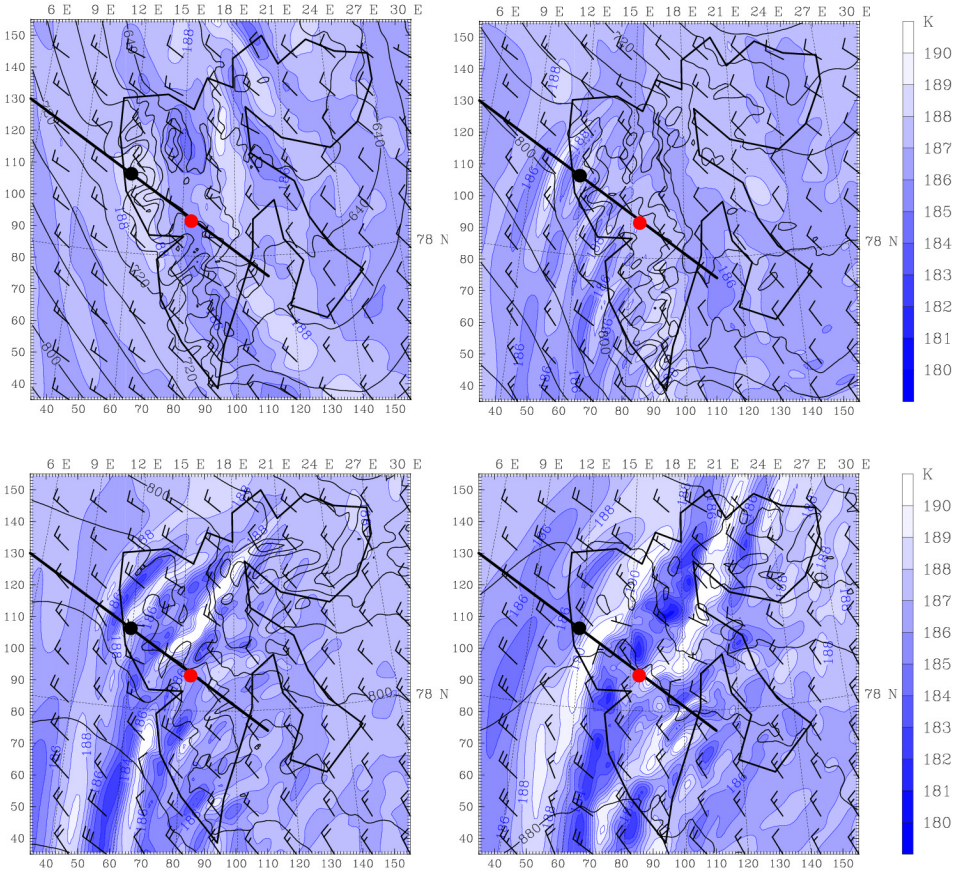

Figure 7. Simulated mesocale temperature (color shading, K) and horizontal wind speed (m/s) (wind flags: small barbs, 5 m/s; long barbs, 10 m/s) at 20 km altitude. The solid contour lines mark the geopotential height of the 900 hPa surface indicating the near-surface flow conditions. Valid times are (top) 26 January 2005 at 0600 and 1200 UTC and (bottom) 1700 and 2100 UTC. Numerical results are from the innermost nested domain with Δx = 4 km. The solid dot marks Ny-Ålesund, while the red dot provides the balloon burst point and descent location of the hygrometer.

relatively short waves only needed about 1 hour assuming mean values of V_H = 30 ms^{-1} and N = 0.02 s^{-1}.

[30] It is interesting to note that the mountain waves seem preferentially to propagate into the direction of higher horizontal wind speed, see horizontal sections at 1200 and 1700 UTC in Figure 7, respectively. This again is in accordance with linear wave theory which predicts the amplitude of internal gravity waves being proportional to the magnitude of the horizontal wind speed. Thus the impact of the mountain waves on the stratospheric temperature field is indeed maximal on the high wind speed side of the aligned tropopause and stratospheric jets (or, in other words: at the inner edge of the polar vortex). During the following hours, the wave and temperature fields changed dramatically: horizontally longer waves with smaller c_{gz} values dominated and the peak-to-peak amplitude of the temperature fluctuations grew to values of $\Delta T \approx 12$ K leading to $T_{\mathrm{MIN}} \approx 181$ K (see Figure 7, 2100 UTC). Whereas the vertical velocity field displays wave propagation throughout the troposphere and stratosphere between 1200 and 1700 UTC, the 2100 UTC vertical section clearly shows the absence of wave modes excited by the flow across Spitsbergen (Figure 8).

[31] Starting at about 1700 UTC, isentropic surfaces began to steepen and gravity wave breaking was simulated between 18 and 22 km altitude in the subsequent period; see the detailed stratospheric temperature fields at 1700 and 2100 UTC in Figure 9. At 1700 UTC, two regions with localized mountain wave–induced cooling below 183 K were located upstream of Ny-Ålesund between 20 and 21.5 km altitude, respectively. Subsequent wave overturning and the attenuated wave forcing due to the weaker tropospheric wind reduced the stratospheric mesoscale temperature anomalies upstream of Ny-Ålesund until 2100 UTC.

[32] Given the strongly nonlinear wave breaking in concert with the time-dependent wave forcing as well as the limited stratospheric data, it is overly ambitious to compare quantitative details of the observed and modeled gravity waves. Furthermore, inaccuracies of the simulated flow (e.g., parameterized mixing might have changed the simulated temperature field irreversibly in an unrealistic manner) produce numerical artifacts which can obscure physical effects.

[33] We conclude that the mesoscale numerical simulations unambiguously demonstrated the short-term presence of mountain wave–induced stratospheric temperature

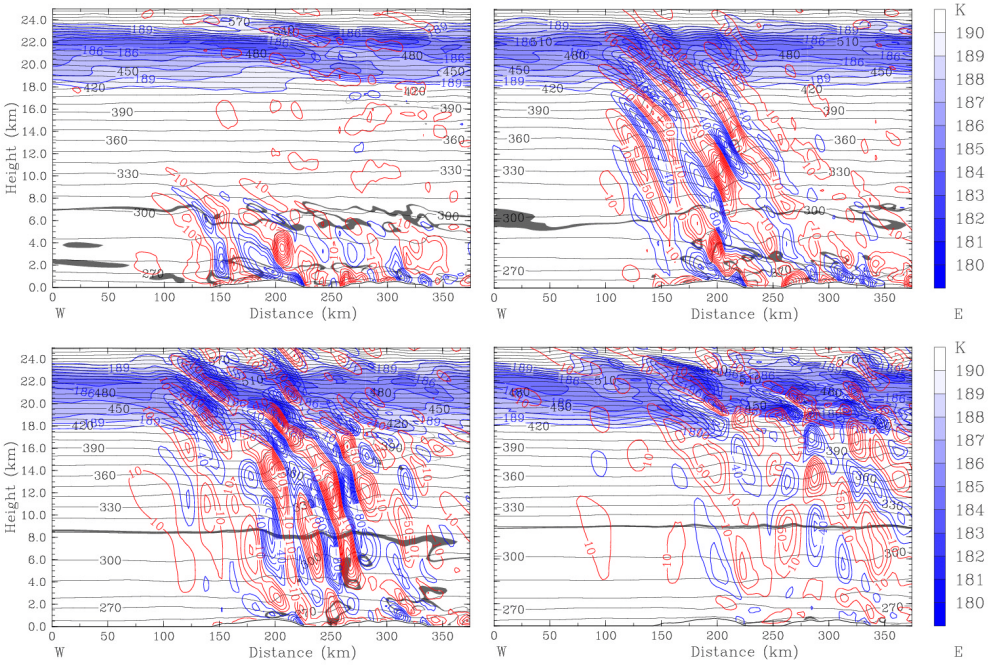

Figure 8. Vertical cross section parallel to the jet axis along the baseline sketched in Figure 6. MM5 simulated vertical wind (blue/red contour lines, cm/s; Δw = 10 cm/s) and potential temperature Θ (solid lines, K; $\Delta\Theta$ = 10 K). The stratospheric cold layer is color shaded with superimposed contour lines of absolute temperature (K; ΔT = 1 K). The location of the dynamical tropopause is indicated by the dark shaded band enclosing the 1.5 and 2.5 PVU surfaces. Times are as in Figure 6; numerical results are from the innermost nested domain with Δx = 4 km. Ny-Ålesund is located at about 160 km.

anomalies with localized temperatures low enough to explain the formation of ice PSCs above Spitsbergen.

5. PSC Formation Scenarios

[34] In order to investigate whether homogeneous freezing was responsible for the PSC occurrence, we calculated the ice saturation ratio $S_i = p_w/p_{sat}(T)$, where p_w is the partial pressure of water vapor and p_{sat} is the saturation vapor pressure over a plane ice surface, calculated after *Sonntag* [1990] [see also *Murphy and Koop*, 2005] along backward trajectories. Furthermore, the freezing threshold saturation ratio S_{cr} for homogeneous nucleation of ice crystals from supercooled aqueous solution droplets [*Koop et al.*, 2000] was computed using the approximation by *Kärcher and Lohmann* [2002]. In the temperature range between 184 K and 190 K, S_{cr} is nearly constant and amounts to about 1.7, i.e., homogeneous freezing requires large ice supersaturation.

[35] Figure 10 depicts the ratio S_i/S_{cr} both for synoptic-scale as well as mesoscale backward trajectories during the last 24 hours and 3 hours, respectively. The mesocale backward trajectories were computed using the half-hourly output of the MM5 simulations. Although the synoptic-scale temperature decreases gradually by about 4 K during 24 hours in the relevant altitude range from 50 hPa (~19 km) to 30 hPa (~22 km) and S_i is larger than 1, the ice saturation ratio S_i never exceeds the threshold S_{cr} (Figure 9 (top)). Air parcels released 3 hours later at the same locations experienced a similar temperature history and S_i/S_{cr} was less than one all the time. Only when we decreased the temperature along the backward trajectories artificially by 2 K, the air parcels released at 30 hPa and 40 hPa achieved $S_i \approx 1.1 \times S_{cr}$ during the first 3 hours after departure. Thus the T511/L60 ECMWF analyses had to be wrong by 2 K to allow homogeneous nucleation by synoptic-scale cooling.

[36] In contrast, S_i values calculated along mesoscale backward trajectories exceeded the threshold for ice nucleation S_{cr}, reaching $S_i \approx 1.4 \times S_{cr}$ due to adiabatic cooling of up to −15 K/h in the uplift regions of the mountain waves (see Figure 9 (bottom)). Altogether, mesoscale trajectories were released at 121 horizontal locations in an 80 km × 80 km grid (see Figure 7 at 1700 UTC) and on 10 vertical levels every hour between 1600 UTC and 2000 UTC. The temporal evolution of S_i/S_{cr} and T of all mesoscale trajectories launched close to Ny-Ålesund showed similar characteristics: (1) S_i never exceeded S_{cr} along trajectories for $p < 30$ hPa as well as for $p > 55$ hPa; (2) the maximum supersaturation was reached for parcels released between 45 and 50 hPa (~19 to 20 km altitude), the actual height of maximum supersaturation was usually 500 to 800 m higher due to wave-induced uplift; (3) maximum values of S_i/S_{cr} were achieved for trajectories released at 1800 UTC and 1900 UTC, while $S_i/S_{cr} > 1$ is rarely achieved for trajectories released before and after; and (4) the typical simulated time of freezing conditions $S_i/S_{cr} > 1$ amounts to about 10 to 20 min and took place during the first 30 min (see Figure 10b).

[37] Backward trajectories released further downstream of Ny-Ålesund at locations close to the balloon observations revealed a much more complex history as the air parcels

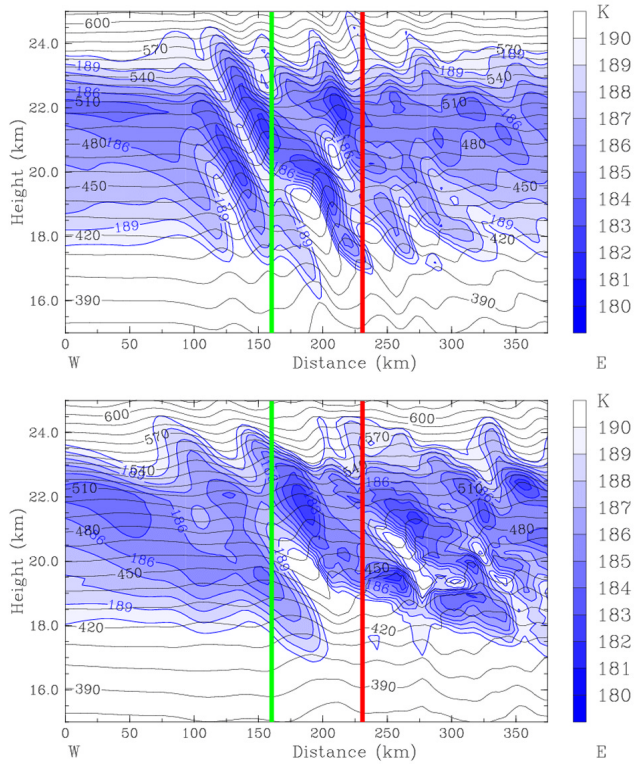

Figure 9. Enlargement of the stratospheric temperature structure between 15 and 25 km from Figure 7 at (top) 1700 UTC (+29 hours since MM5 initialization) and at (bottom) 2100 UTC (+33 hours since MM5 initialization), with the location of the measured profile by lidar (green line) and the FLASH-B hygrometer (red line).

passed several mesoscale temperature maxima and minima. Almost all stratospheric levels experienced conditions where the critical value S_{cr} was exceeded for several times in the first three hours after release. Thus the lidar as well as the H_2O observations show probably growing or decaying ice PSC layers depending on the actual temperature and the temperature history along the trajectories. It is interesting to note that the possibility of precipitating ice particles from upper layers to the layers below 30 hPa can be excluded, as all upper trajectories never attained values of $S_i/S_{cr} > 1$.

[38] Microphysical calculations of the H_2O depletion by growing ice crystals have been performed. As the large water vapor depletion of 1.5 ppmv could not have been caused by NAT particles due to the limited availability of HNO_3 in the order of a few ppbv, the calculations were limited to the growth of water ice particles.

[39] At time $t = 0$, a number density $n_i = 1$, 5, 10, 50, 100, and 500 ice crystals per cm^3 with an initial mass of 10^{-16} kg were assumed to freeze at $T_{HOM} = 182.6$ K for $q_{H20} = 5$ ppmv and $T_{HOM} = 183.6$ K for $q_{H20} = 6$ ppmv background water vapor concentration; the values of T_{HOM} correspond to the temperature threshold for homogeneous freezing. Subsequently, the diffusive growth of the ice crystals reduces the ambient water vapor. The growth rates for the ice crystals were calculated according to *Pruppracher and Klett* [1978, chap. 13.3]. In order to simulate the maximum observed depletion of up to 1.5 ppmv, number densities $n_i > 10$ cm^{-3} are necessary. In case of homogeneous nucleation, these high number densities are generated under cooling rate conditions that are equivalent to vertical wind velocities $w > 0.1$ ms^{-1} [see *Kärcher and Lohmann*, 2002, Figure 3]. These values correspond closely to our typical simulated mesoscale values of $|w_{MAX}| \approx 0.5$ ms^{-1}; excep-

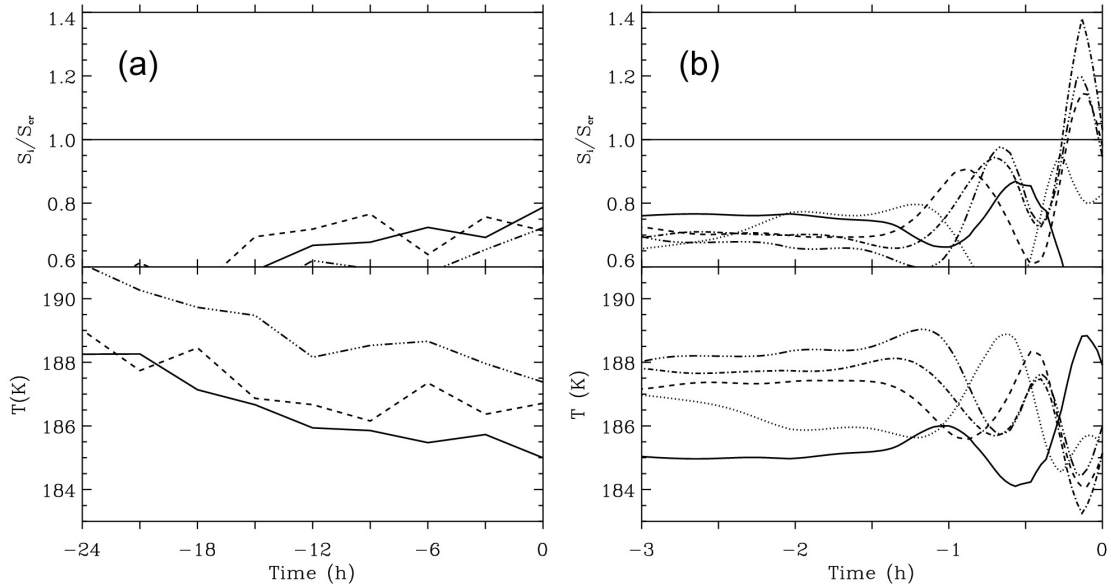

Figure 10. Ratio of the ice saturation ratio S_i to the threshold value S_{cr}, where homogeneous nucleation occurs, and temperature (K) along (a) synoptic-scale and (b) mesoscale backward trajectories released at Ny-Ålesund on 26 January 2005 at 1800 UTC (T511/L60 ECMWF) (Figure 10a) and 1900 UTC (MM5) (Figure 10b). The pressure at the departure levels for ECMWF backward trajectories is 30 hPa (solid lines), 40 hPa (dashed lines), and 50 hPa (dash-triple-dotted lines) and for the mesoscale backward trajectories 32.2 hPa (solid lines), 36.8 hPa (dotted lines), 41.6 hPa (dashed lines), 46.5 hPa (dash-dotted lines), and 51.4 hPa (dash-triple-dotted lines), respectively.

tionally, maximum values $w > 1.2\ \mathrm{ms}^{-1}$ were calculated along individual trajectories. The calculation shows that 1.5 ppmv of water vapor can indeed be reduced in less then 45 min.

[40] Summarizing, the adiabatic cooling and homogeneous freezing in mesoscale mountain waves could explain the formation of the ice PSCs around Ny-Ålesund whereas homogeneous nucleation of ice particles due to synoptic-scale cooling along trajectories is very unlikely.

[41] Heterogeneous freezing requires generally lower ice supersaturations S_i in the temperature range of about 185 K [*DeMott et al.*, 2003]. Assuming $S_i \approx 1.3$, similar microphysical simulations as for the homogeneous freezing, whereby n_i now represents the initial concentration of activated ice nuclei, reveal that even higher number concentrations $n_i > 50\ \mathrm{cm}^{-3}$ and much longer times spans would be necessary for reducing the water vapor by 1.5 ppmv. As recent in situ observations of total number concentrations of aerosol particles show $n_i \approx 10$ to 20 cm^{-3} in an altitude range between 18 and 20 km, the requirements are hardly met. Yet, the enhanced fraction of nonvolatile particles (meteoritic dust) inside the polar vortex might increase heterogeneous nucleation rates [*Curtius et al.*, 2005]. These particles or micrometeorites have been recently suggested to be suitable candidates for the nucleation of PSCs consisting of low number densities of large NAT particles [*Voigt et al.*, 2005]. However, scientific knowledge on the actual heterogeneous freezing processes in the stratosphere is limited, hence, we leave it open whether this process might explain the formation of the observed ice PSC.

6. Conclusion

[42] On 26 January 2005, an ice PSC with backscatter ratio $R_{532\mathrm{nm}} > 10$ and volume depolarization $\delta_{532\mathrm{nm}} > 50\%$ was observed at Ny-Ålesund, Spitsbergen, under exceptional meteorological conditions. This fortunate event is unique within the 15 year data record of the German lidar observations and confirms the documented rareness of NAT enhanced PSCs [*Massoli et al.*, 2006]. Moreover, simultaneous balloon-borne measurements of depleted layers of stratospheric water vapor indicate that freezing produced a sufficiently large number of ice particles, hence, the presence of ice PSCs further downstream of Ny-Ålesund. However, the paucity of sufficient experimental information on the upstream stratospheric conditions and on the availability of ice nuclei does not allow a final conclusion about the actual ice PSC formation processes.

[43] Even so, the synoptic-scale and mesoscale temperature analyses revealed that the ice PSCs most likely formed locally and shortly before the observation. In addition, the fine structure in the observed stratospheric profiles of $R_{532\mathrm{nm}}$, $\delta_{532\mathrm{nm}}$, q_{H2O}, and temperature indicate the presence of small-scale processes in the PSC region such as mountain waves. Thus we favor the scenario of ice PSC formation provoked by mesoscale temperature fluctuations. In this scenario, the prevailing synoptic wave activity provided the necessary background conditions that brought the stratospheric temperature below the frost point T_{ice}.

[44] The exceptional synoptic situation responsible for this event was characterized by the combination of three closely linked processes: (1) the passing tropospheric cold front (see Appendix A) with strong postfrontal northwesterly flow past Spitsbergen's mountains excited the mountain waves; (2) the unusual location and orientation of the tropopause jet due to the northward extending high-pressure ridge behind the frontal system led to an alignment with the lower tropospheric winds and favored vertically upward gravity waves propagation into the stratosphere; and finally, (3) the presence of the vortex cold pool in the baroclinically deformed polar vortex above Spitsbergen (see schematic in Figure 11).

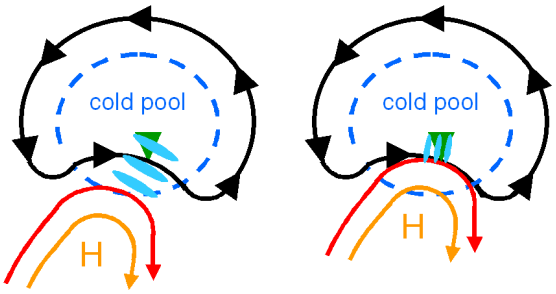

Figure 11. Schematic of the synoptic situation on 26 January 2005, illustrating the conditions (left) for inertia-gravity waves induced by the jet stream and (right) for mountain gravity waves.

[45] The extent to which the occurrence of ice PSCs may affect the water vapor distribution on a vortex-wide scale depends on their spatial extent, their lifetime and on the particle size distribution. On 26 January 2005, the conditions for ice PSC formation above Spitsbergen were given for a short period of less than 12 hours. Occasional warming of air parcels in mesoscale wave troughs might even limit this time considerably. Considering the growth time from particle formation to gravitational settling, the potential dehydration caused by the ice PSC observed above Spitsbergen is marginal. Although we cannot exclude that the long-lasting mountain wave event above Greenland caused a large-scale dehydration south of Spitsbergen and in other parts of the polar vortex [*Jiménez et al.*, 2006], we find that the observed H_2O reduction above Spitsbergen was a local event.

[46] Monitoring the Arctic water vapor distribution by satellite-borne instruments in conjunction with spatially high-resolved meteorological analyses might answer the question whether mesoscale events can influence the water vapor budget of the Arctic stratosphere significantly.

Appendix A

[47] The two days before the lidar observations were characterized by strong gusty winds and low-level clouds associated with a storm system. This low developed in the period starting on 24 January 2005 where an explosive cyclogenesis event (surface pressure drop of 30 hPa in only 24 hours) occurred over the Atlantic between Greenland and Spitsbergen. The low-pressure system with a minimum surface pressure of 973.5 hPa passed the station one day before the observation on 25 January 2005 with the subsequent cold front passage at about 2200 UTC. The Koldewey meteorological ground station registered a sharp drop of the

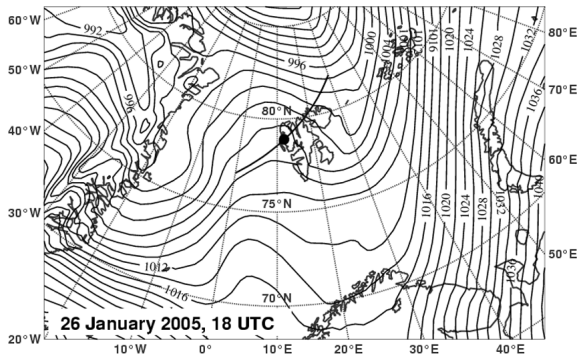

Figure A1. ECMWF-analyzed mean sea level pressure valid on 26 January 2005 at 1800 UTC. The solid line crossing Ny-Ålesund (marked by a black dot) sketches the baseline of the vertical section shown in Figure 5.

ground temperature from about −2.5°C to about −10°C within 1.5 hours.

[48] Thus on 26 January 2005, cold Arctic air dominated the tropospheric conditions in Ny-Ålesund. The ground pressure rose constantly during the day due to the approaching high-pressure ridge while the surface wind speed decreased gradually from 15 ms^{-1} at 0000 UTC to about 2 ms^{-1} at the time of the observation at 1900 UTC. Very low clouds with snow showers were present all morning and afternoon, while the ground temperature (about −12°C) and wind direction (from northwest) remained more or less constant. Furthermore, the 1100 UTC radiosonde measurements revealed a wind direction roughly uniform from northwest throughout the troposphere and lower stratosphere and the thermal tropopause being located at 6.5 km (not shown).

[49] At the evening of 26 January 2005, Ny-Ålesund was located east of the ridge axis (see Figure A1) and nearly westerly winds dominated the near-surface flow field. Owing to the descent under high-pressure conditions, the formerly uniform low-level clouds broke up and allowed the lidar measurements. In the lower part of the troposphere, the 2300 UTC radiosonde measurements revealed much weaker wind and its direction turned to southwesterlies. The thermal tropopause was now located at an altitude of 9 km and, in contrast to the 1100 UTC sounding, it was very sharp as usually observed under anticyclonic conditions.

Appendix B

[50] The mesoscale meteorological fields are calculated with the nonhydrostatic weather prediction model MM5 version 3.4 [*Dudhia*, 1993; *Dudhia et al.*, 2001] (available at http://www.mmm.ucar.edu/mm5). The outer model domain is centered at (78.5°N, 17°E) with an extension of 1092 km × 1092 km. In this domain a horizontal grid size of Δx = 12 km is used. A local grid refinement scheme with a nested domain of 4 km horizontal resolution is applied to resolve most of the horizontal wave number spectrum of gravity waves excited either by the orography or by jet stream instabilities. In the vertical direction 150 levels up to the model top at 10 hPa ($\Delta z \approx$ 200 m) are applied. Turbulent and moist processes are accounted for by standard schemes as turbulence parameterization [*Hong and Pan*, 1996], *Grell et al.*'s [1994] cumulus parameterization, and *Reisner et al.*'s [1998] microphysical scheme. The initial condition on 25 January 2005 at 12 UTC and the boundary values of the model integration were prescribed by operational analyses of the ECMWF model with a horizontal resolution of 0.5° in latitude and longitude and 15 pressure levels between 1000 hPa and the 10 hPa pressure level.

[51] **Acknowledgments.** We thank the station team in Ny-Ålesund for their effort in lidar operation and dedication to sonde launches. The work was partly funded through the European Commission project SCOUT-O3. The meteorological analysis data were available through the ECMWF special project "Effect of nonhydrostatic gravity waves on the stratosphere above Scandinavia" of one of the authors (A.D.). The MM5 computations were performed at the German High Performance Computing Center for Climate and Earth Research in Hamburg, Germany. We very much appreciate the careful reading, correcting, and commenting of the manuscript by Christiane Voigt (DLR) and Peter Spichtinger (ETH Zürich). Their thorough knowledge of microphysical processes helped us to understand and interpret the observations and numerical simulation results in a much more comprehensive way.

References

Beyerle, G., R. Neuber, O. Schrems, F. Wittrock, and B. Knudsen (1994), Multiwavelength lidar measurements of stratospheric aerosols above Spitsbergen during winter 1992/1993, *Geophys. Res. Lett.*, *21*, 57–60.

Biele, J., A. Tsias, B. P. Luo, K. S. Carslaw, R. Neuber, G. Beyerle, and T. Peter (2001), Nonequilibrium coexistence of solid and liquid particles in Arctic stratospheric clouds, *J. Geophys. Res.*, *106*, 22,991–23,007.

Browell, E. V., C. F. Butler, S. Ismail, P. A. Robinette, A. F. Carter, N. S. Higdon, O. B. Toon, M. R. Schoeberl, and A. F. Tuck (1990), Airborne lidar observations in the wintertime Arctic stratosphere: Polar stratospheric clouds, *Geophys. Res. Lett.*, *17*, 385–388.

Buss, S., A. Hertzog, C. Hostetler, T. P. Bui, D. Lüthi, and H. Wernli (2004), Analysis of a jet stream induced gravity wave associated with an observed stratospheric ice cloud over Greenland, *Atmos. Chem. Phys.*, *4*, 1183–1200.

Carslaw, K. S., et al. (1998a), Increased stratospheric ozone depletion due to mountain-induced atmospheric waves, *Nature*, *391*, 675–678.

Carslaw, K. S., M. Wirth, A. Tsias, B. P. Luo, A. Dörnbrack, M. Leutbecher, H. Volkert, W. Renger, J. T. Bacmeister, and T. Peter (1998b), Particle microphysics and chemistry in remotely observed mountain polar stratospheric clouds, *J. Geophys. Res.*, *103*, 5785–5796.

Curtius, J., et al. (2005), Observations of meteoric material and implications for aerosol nucleation in the winter Arctic lower stratosphere derived from in situ particle measurements, *Atmos. Chem. Phys.*, *5*, 3053–3069.

DeMott, P. J., D. J. Cziczo, A. J. Prenni, D. M. Murphy, S. M. Kreidenweis, D. S. Thomson, R. Borys, and D. C. Rogers (2003), Measurements of the concentration and composition of nuclei for cirrus formation, *Proc. Natl. Acad. Sci. U. S. A.*, *100*, 14,655–14,660.

Dörnbrack, A. (1998), Turbulent mixing by breaking gravity waves, *J. Fluid Mech.*, *375*, 113–141.

Dörnbrack, A., and M. Leutbecher (2001), Relevance of mountain waves for the formation of polar stratospheric clouds over Scandinavia: A 20 year climatology, *J. Geophys. Res.*, *106*, 1583–1593.

Dörnbrack, A., M. Leutbecher, R. Kivi, and E. Kyrö (1999), Mountain wave induced record low stratospheric temperatures above northern Scandinavia, *Tellus, Ser. A*, *51*, 951–963.

Dörnbrack, A., T. Birner, A. Fix, H. Flentje, A. Meister, H. Schmid, E. V. Browell, and M. J. Mahoney (2002), Evidence for inertia gravity waves forming polar stratospheric clouds over Scandinavia, *J. Geophys. Res.*, *107*(D20), 8287, doi:10.1029/2001JD000452.

Dudhia, J. (1993), A non-hydrostatic version of the Penn State–NCAR Mesoscale Model: Validation tests and simulation of an Atlantic cyclone and cold front, *Mon. Weather Rev.*, *121*, 1493–1513.

Dudhia, J., D. Gill, Y.-R. Guo, K. Manning, and W. Wang (2001), PSU/NCAR mesoscale modeling system tutorial class notes and user guide: MM5 modeling system version 3, report, Natl. Cent. for Atmos. Res., Boulder, Colo.

Dunkerton, T. J. (1984), Inertia-gravity waves in the stratosphere, *J. Atmos. Sci.*, *41*, 3396–3404.

Fueglistaler, S., S. Buss, B. P. Luo, H. Wernli, H. Flentje, C. A. Hostetler, L. R. Poole, K. S. Carslaw, and T. Peter (2003), Detailed modeling of mountain wave PSCs, *Atmos. Chem. Phys.*, *3*, 697–712.

Gill, A. E. (1982), *Atmosphere-Ocean Dynamics*, 662 pp., Elsevier, New York.

Grell, G. A., J. Dudhia, and D. R. Stauffer (1994), A description of the fifth-generation Penn State/NCAR mesoscale model (MM5), *Tech. Note NCAR/TN-398+STR*, 117 pp., Natl. Cent. for Atmos. Res., Boulder, Colo.

Hansen, G., and U.-P. Hoppe (1997), Lidar observations of polar stratospheric clouds and stratospheric temperature in winter 1995/96 over northern Norway, *Geophys. Res. Lett.*, *24*, 131–134.

Herman, R. L., et al. (2002), Hydration, dehydration, and the total hydrogen budget of the 1999/2000 winter Arctic stratosphere, *J. Geophys. Res.*, *107*, 8320, doi:10.1029/2001JD001257. [printed *108*(D5), 2003]

Hitchman, M. H., M. L. Buker, G. J. Tripoli, E. V. Browell, W. B. Grant, T. J. McGee, and J. F. Burris (2003), Nonorographic generation of Arctic polar stratospheric clouds during December 1999, *J. Geophys. Res.*, *108*(D5), 8325, doi:10.1029/2001JD001034.

Holton, J. R., P. E. Haynes, M. E. McIntire, A. R. Douglas, R. R. Rood, and L. Pfister (1995), Stratosphere-troposphere exchange, *Rev. Geophys.*, *33*, 403–439.

Hong, S.-Y., and H.-L. Pan (1996), Nonlocal boundary layer vertical diffusion in a medium-range forecast model, *Mon. Weather Rev.*, *124*, 2322–2339.

Hu, R.-M., K. S. Carslaw, C. Hostetler, L. R. Poole, B. Luo, T. Peter, S. Füeglistaler, T. J. McGee, and J. F. Burris (2002), Microphysical properties of wave polar stratospheric clouds retrieved from lidar measurements during SOLVE/THESEO 2000, *J. Geophys. Res.*, *107*(D20), 8294, doi:10.1029/2001JD001125.

Jiménez, C., H. C. Pumphrey, I. A. Mackenzie, G. L. Manney, M. L. Santee, M. J. Schwartz, R. S. Harwood, and J. W. Waters (2006), EOS MLS observations of dehydration in the 2004–2005 polar winters, *Geophys. Res. Lett.*, *33*, L16806, doi:10.1029/2006GL025926.

Kärcher, B., and U. Lohmann (2002), A parameterization of cirrus cloud formation: Homogeneous freezing of supercooled aerosols, *J. Geophys. Res.*, *107*(D2), 4010, doi:10.1029/2001JD000470.

Kivi, R., E. Kyrö, A. Dörnbrack, and T. Birner (2001), Observations of vertically thick polar stratospheric clouds and record low temperature in the Arctic vortex, *Geophys. Res. Lett.*, *28*, 3661–3664.

Kleinböhl, A., H. Bremer, H. Küllmann, J. Kuttippurath, E. V. Browell, T. Canty, R. J. Salawitch, G. C. Toon, and J. Notholt (2005), Denitrification in the Arctic mid-winter 2004/2005 observed by airborne submillimeter radiometry, *Geophys. Res. Lett.*, *32*, L19811, doi:10.1029/2005GL023408.

Koop, T., B. Luo, A. Tsias, and T. Peter (2000), Water activity as the determinant for homogeneous ice nucleation in aqueous solutions, *Nature*, *406*, 611–614.

Leutbecher, M., and H. Volkert (2000), The propagation of mountain waves into the stratosphere: Quantitative evaluation of three-dimensional simulations, *J. Atmos. Sci.*, *57*, 3090–3108.

Luo, B. P., C. Voigt, S. Füeglistaler, and T. Peter (2003), Extreme NAT supersaturations in mountain wave ice PSCs: A clue to NAT formation, *J. Geophys. Res.*, *108*(D15), 4441, doi:10.1029/2002JD003104.

Manney, G. L., M. L. Santee, L. Froidevaux, K. Hoppel, N. J. Livesey, and J. W. Waters (2006), EOS MSL observations of ozone loss in the 2004–2005 Arctic winter, *Geophys. Res. Lett.*, *33*, L04802, doi:10.1029/2005GL024494.

Massoli, P., M. Maturilli, and R. Neuber (2006), Climatology of Arctic polar stratospheric clouds as measured by lidar in Ny-Ålesund, Spitsbergen (79°N, 12°E), *J. Geophys. Res.*, *111*, D09206, doi:10.1029/2005JD005840.

Morgan, M. C., and J. W. Nielsen-Gammon (1998), Using tropopause maps to diagnose midlatitude weather systems, *Mon. Weather Rev.*, *126*, 2555–2579.

Murphy, D. M., and T. Koop (2005), Review of the vapour pressures of ice and supercooled water for atmospheric applications, *Q. J. R. Meteorol. Soc.*, *131*, 1539–1565.

Nedoluha, G. E., R. M. Bevilacqua, K. W. Hoppel, M. Daehler, E. P. Shettle, J. H. Hornstein, M. D. Fromm, J. D. Lumpe, and J. E. Rosenfield (2000), POAM III measurements of dehydration in the Antarctic lower stratosphere, *Geophys. Res. Lett.*, *27*, 1683–1686.

Nedoluha, G. E., R. M. Bevilacqua, and K. W. Hoppel (2002), POAM III measurements of dehydration in the Antarctic and comparison with the Arctic, *J. Geophys. Res.*, *107*(D20), 8290, doi:10.1029/2001JD001184.

O'Sullivan, D., and T. J. Dunkerton (1995), Generation of inertia-gravity waves in a simulated life cycle of baroclinic instability, *J. Atmos. Sci.*, *52*, 3695–3716.

Peters, D., and D. W. Waugh (1996), Influence of barotropic shear on the poleward advection of upper tropospheric air, *J. Atmos. Sci.*, *53*, 3013–3031.

Plougonven, R., and H. Teitelbaum (2003), Comparison of a large-scale inertia-gravity wave as seen in the ECMWF analyses and from radiosondes, *Geophys. Res. Lett.*, *30*(18), 1954, doi:10.1029/2003GL017716.

Plougonven, R., H. Teitelbaum, and V. Zeitlin (2003), Inertia gravity wave generation by the tropospheric midlatitude jet as given by the Fronts and Atlantic Storm-Track Experiment radio soundings, *J. Geophys. Res.*, *108*(D21), 4686, doi:10.1029/2003JD003535.

Pruppacher, H. R., and J. D. Klett (1978), *Microphysics in Clouds and Precipitation*, 714 pp., Springer, New York.

Reichardt, J., A. Dörnbrack, S. Reichardt, P. Yang, and T. J. McGee (2004), Mountain wave PSC dynamics and microphysics from ground-based lidar measurements and meteorological modeling, *Atmos. Chem. Phys.*, *4*, 1149–1165.

Reisner, J., R. J. Rasmussen, and R. T. Bruintjes (1998), Explicit forecasting of supercooled liquid water in winter storms using the MM5 mesoscale model, *Q. J. R. Meteorol. Soc.*, *124B*, 1071–1107.

Rex, M., et al. (1997), Prolonged stratospheric ozone loss in the 1995–96 Arctic winter, *Nature*, *389*, 835–838.

Schiller, C., et al. (2002), Dehydration in the Arctic stratosphere during the SOLVE/THESEO-2000 campaigns, *J. Geophys. Res.*, *107*(D20), 8293, doi:10.1029/2001JD000463.

Solomon, S. (1999), Stratospheric ozone depletion: A review of concepts and history, *Rev. Geophys.*, *37*, 275–316.

Sonntag, D. (1990), Important new values of the physical constants of 1986, vapour pressure formulations based on the ITS-90, and psychrometer formulae, *Z. Meteorol.*, *40*, 340–344.

Spichtinger, P., K. Gierens, and A. Dörnbrack (2005), Formation of ice supersaturation by mesoscale gravity waves, *Atmos. Chem. Phys.*, *5*, 1243–1255.

Teitelbaum, H., and R. Sadourny (1998), The role of planetary waves in the formation of polar stratospheric clouds, *Tellus, Ser. A*, *50*, 302–312.

Teitelbaum, H., M. Moustaoui, and M. Fromm (2001), Exploring polar stratospheric cloud and ozone minihole formation: The primary importance of synoptic-scale flow perturbations, *J. Geophys. Res.*, *106*, 28,173–28,188.

Toon, O. B., E. V. Browell, S. Kinne, and J. Jordan (1990), An analysis of lidar observations of polar stratospheric clouds, *Geophys. Res. Lett.*, *17*, 393–396.

Tsias, A., et al. (1999), Aircraft lidar observations of an enhanced type Ia PSc during APE-POLECAT, *J. Geophys. Res.*, *104*, 23,961–23,969.

Voigt, C., et al. (2005), Nitric acid trihydrate (NAT) formation at low NAT supersaturation in polar stratospheric clouds (PSCs), *Atmos. Chem. Phys.*, *5*, 1371–1380.

Vömel, H., M. Rummukainen, R. Kivi, J. Karhu, T. Turunen, E. Kyrö, J. Rosen, N. Kjome, and S. Oltmans (1997), Dehydration and sedimentation of ice particles in the Arctic stratospheric vortex, *Geophys. Res. Lett.*, *24*, 795–798.

Waibel, A. E., T. Peter, K. S. Carslaw, H. Oelhaf, G. Wetzel, P. J. Crutzen, U. Pöschl, A. Tsias, E. Reimer, and H. Fischer (1999), Arctic ozone loss due to denitrification, *Science*, *283*, 2064–2069.

Wernli, H., and H. C. Davis (1997), A Lagrangian-based analysis of extratropical cyclones. I: The method and some applications, *Q. J. R. Meteorol. Soc.*, *123*, 467–489.

Wirth, M., A. Tsias, A. Dörnbrack, V. Weiß, K. S. Carslaw, M. Leutbecher, W. Renger, H. Volkert, and T. Peter (1999), Model-guided Lagrangian observation and simulation of mountain polar stratospheric clouds, *J. Geophys. Res.*, *104*, 23,971–23,981.

Yushkov, V., S. Merkulov, and V. Astakhov (1998), Optical balloon hygrometer for upper stratosphere and stratosphere water vapor measurements, *Proc. SPIE*, *3501*, 439–445.

Yushkov, V., N. Sitnikov, I. Zaitsev, J.-P. Pommereau, and A. Garnier (2001), Stratospheric water vapor measurements in the winter arctic with optical fluorescent hygrometer on short and long duration balloons, in *Proceedings of the 15th ESA Symposium on European Rocket and Balloon Programmes and Related Research*, *ESA-SP-471*, edited by B. Warmbein, pp. 263–268, Eur. Space Agency, Noordwijk, Netherlands.

Zhang, F. (2004), Generation of mesoscale gravity waves in upper-tropospheric jet-front systems, *J. Atmos. Sci.*, *61*, 440–457.

Zülicke, C., and D. Peters (2006), Simulation of inertia-gravity waves in a poleward breaking Rossby wave, *J. Atmos. Sci.*, in press.

A. Dörnbrack, DLR Oberpfaffenhofen, Institut für Physik der Atmosphäre, Münchner Str. 20, D-82230 Wessling, Germany.

M. Maturilli, Alfred Wegener Institute for Polar and Marine Research, Telegrafenberg A43, D-14473 Potsdam, Germany. (mmaturilli@awi-potsdam.de)